Porosity calculations and permeability simulations in a biolithite rock using x-ray tomography images

Porosity and permeability calculations in a Biolithite using x-ray tomography images

Adetomiwa Aderemi, Elli-Maria Charalampidou, Zeyun Jiang, Heriot-Watt University.*
Erika Tudisco, Lund University.

Summary

Engineering energy storage/extraction for geoenergy applications (e.g., geothermal energy extraction, CO_2 and/or Hydrogen storage) requires a very good knowledge of subsurface heterogeneities. One of the principal factors that influences the response of the underground system is the continuously evolving pore networks of the targeted rocks. This work aims to understand the pore network of a natural Biolithite (Figure 1), coming from a Greek outcrop, and to predict the permeability of lab-scale systems (due to diagenetic alterations and/or natural deformation) using x-ray computed tomography (CT) images (3D) and stochastic model reconstructions. We emphasize on the importance of a reproducible image analysis workflow (Figure 2) during reservoir description, as an input to extracting pore network models that have representative geometrical and topological characteristics at core-plug scale.

Introduction

Successful characterization of carbonates starts from properly describing them by using globally defined classification standards (among others Folk, 1959; Dunham & Ham, 1962). Carbonates are susceptible to physicochemical reactions after deposition, though over a long period of time, these can alter the internal architecture of the rock creating complex pore networks and connectivity.

X-ray CT is a method widely used in the non-destructive investigation of the internal architecture of rock fabric. 3D digital images can be used to create pore network models with the aid of novel extraction computer algorithms.

The ability to reconstruct representative models of the pore network from x-ray CT images at different length scales unlocks a better understanding of spatial continuity of porosity and permeability and can be useful in deriving realizations of some rock and fluid properties in porous media such as capillary pressure, wettability, relative permeability, acoustic velocity, etc., which also control the behavior of lithological layers when subjected to stress or dynamic conditions (i.e., fluid production/injection).

Image analysis workflow

X-ray CT images (50µm resolution) were acquired (at Lund University) from three cylindrical Biolithite plug samples cored in three different directions (Figure 1). Higher resolution (10µm) images were further acquired on one of the samples – B23. The scanned samples had not been previously subjected to any lab-induced deformation.

Table 1: Summary of acquired image properties.

Title	Width (X)	Length (Y)	Depth (Z= slice number)	Size	Display range	Voxel size (xyz)	Scale
	(Voxels)			(GB)	(gray values)	(pixel^3)	(pixels/mm)
B11	691	691	1371	1.2	17427 - 55381	1 X 1X 1	18.18
B23	673	670	1442	1.2	0 - 65535		17.71
B23_HR	1004	1024	894	1.7	0 - 65535		26.00
B33	673	670	1470	1.2	0 - 65535		17.71

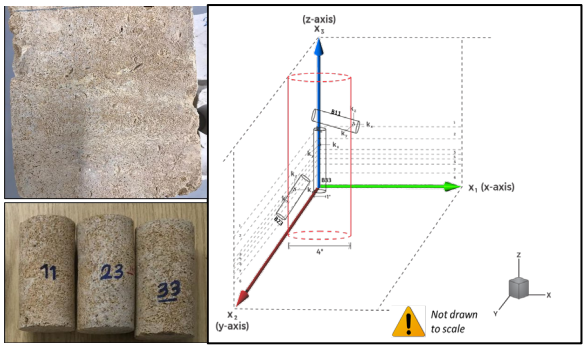

Figure 1: Biolithite samples and conceptual schematic of multilayered carbonate.

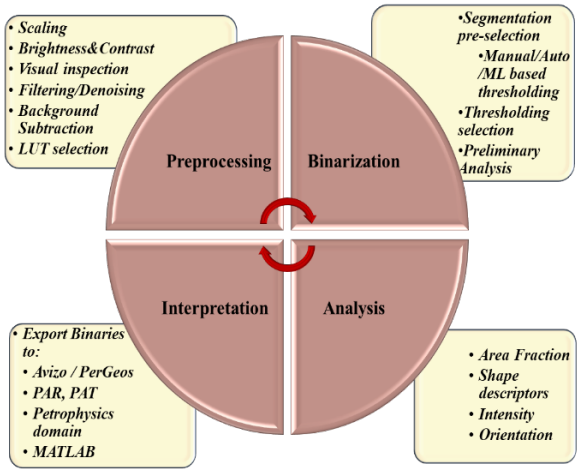

Figure 2: Workflow followed in this study.

Porosity and permeability calculations in a Biolithite using x-ray tomography images

The 3D digital images were pre-processed to reduce noise and facilitate the segmentation that followed-up. An important aspect of the pre-processing was the background subtraction. A study by Aaron, J., & Chew, T. 2021 defined the background in image analysis as any detected but non-informative signal, whose presence may render subsequent analysis inaccurate or otherwise misleading due to un-even illumination in the background of the image during acquisition.

A plot profile of the final conditioned 3D stack was used to understand relationships between the x-ray intensity, matrix, and pores. A normalized color scale on all samples, with modified display ranges, was used for better visualization of the internal architecture complexity of this Biolithite. Figure 3 shows the importance of pre-processing on the quality of final image before analysis and interpretation. On all raw grayscale displays with examples in Figure 4, the matrix (lighter colors) has higher intensity, while the pores (in darker colors) have lower intensity. On the final processed display, two categories of pore-related features were observed on all images: magenta-cyan-navy blue, and a composite of black-red-green. The white and yellow color bands were correlated to the matrix. The rules set up for classification depend on the choice of grayscale ranges and determine the magnitude of porosity that is eventually calculated. The classification of trends and cluster analysis of the pores and matrix was performed using the Trainable Weka segmentation, a Java-based repository of machine learning algorithms. Labelled, binarized image volumes were then used to extract the pore network of each plug sample. Total porosity was calculated as the ratio of the area of each thresholded object to non-objects within a region of interest using the binarized 3D images.

Pore anisotropy was investigated within a subset volume using the 'OrientationJ' plugin in Fiji – it uses a structure tensor calculated for each pixel in the image, by sliding a Gaussian analysis window - slice by slice throughout the whole stack (Clemons, et al., 2018). Local orientation properties were calculated and visualized as color images with the orientation encoded using a color map legend to indicate the axis when viewing a 2D slice (Figure 4b). Orientation magnitudes were crossplotted with Feret X & Y parameters to highlight the spatial position and relationship of pore clusters in the image stack (Figure 5c and d). The permeability tensor was calculated using the Pore Analysis Tools and the binarized images as input parameters. This calculation involves a) getting the 3D Euclidean distance map; b) voxel clustering; c) pore network space extraction; d) pore space partitioning; e) computing shape factor (Jiang et al., 2007).

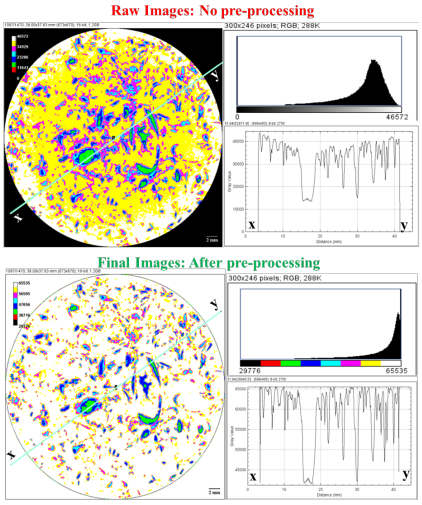

Figure 3: B33 Raw and Final Images.

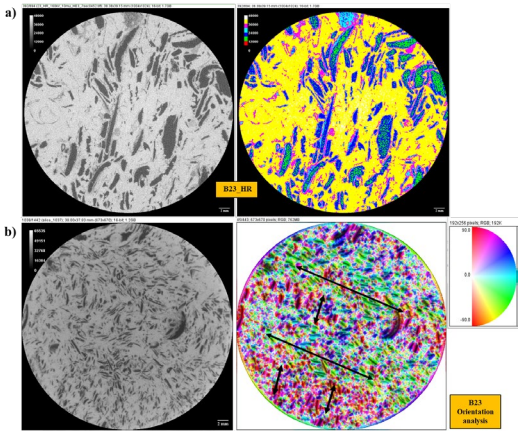

Figure 4: Orientation in B23_HR (a) and B23 (b) samples.

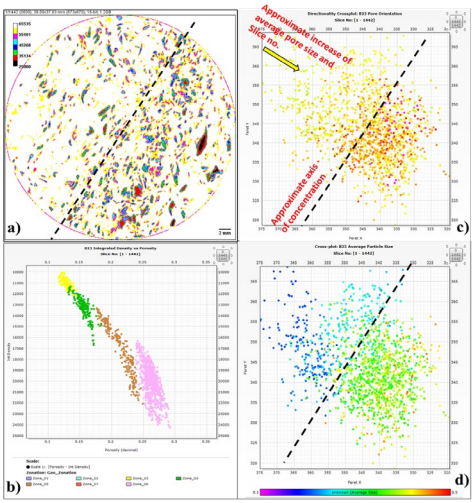

Figure 5: An example of B23 sample interpretation.

Porosity and permeability calculations in a Biolithite using x-ray tomography images

Results & Discussion

In the absence of additional information such as scanning electron microscope (SEM) images etc., we explored the textural/diagenetic features within this carbonate by combining them with the spatial geometrical relationship of the pore spaces and observations from previous works (among others Folk, 1959, Choquette & Pray, 1970 Lokier & Al Junaibi, 2016, Li, et al., 2020, Sun, et al., 2021, Ranjbar-Karami, et. al., 2021), which describes several pore facies with illustrations and images. An interplay of interparticle and moldic porosity is inferred based on x-ray CT data alone.

The spatial relationship of interparticle and moldic porosities are inferred to be the main factor controlling permeability at this resolution; the smaller-sized pores contributing more to the permeability. The samples in this study have porosity between 18 and 30% measured from image analysis. Permeability varies between 0.1 and 70md. A plot of the 3D volume distribution of the extracted pore network shows that the sample is dominated by small sized pores. The larger, isolated pore sizes are estimated to be about 30-40% of the total porosity, while 60-70% is attributed to smaller, well-connected pores.

The pore geometry in sample B11 is elongated, and well sorted. B23 has similar characteristics but has a preferential alignment distributed along certain spatial clusters, which coincides with an increase in average pore size along the 'depth' axes as seen in Figure 5c and d. No fractures, attributed to preferential alignment, are observed in this sample. It is unclear whether the observed pore anisotropy in sample B23 is due to local structural trends, depositional processes, or the direction in which the plugs were cut from the core. Zones which correlate to 'porosity facies' in each plug sample (Figure 6), were created using integrated density (Figure 5b) and mean intensity crossplotted with porosity. Higher correlation coefficients in each 'pore facies' are related to lower variability of pore sizes as observed for samples B11 and B23. B33 shows lower correlation coefficients with pores more randomly distributed, while crossplots of Feret X-Y with various properties in the z-scale show no trend.

The choice of data preprocessing steps, gray value ranges - derived from pore/matrix feature characteristics, cropping to a region of interest before image analysis, etc. were observed to have an impact of up to ±30% uncertainty of porosity results in these samples. Although results from different binarization methods (Table 2) reveal that K_z has the highest magnitude in all cases, lower magnitudes of permeability were calculated in sample B33 using zones from the porosity correlation (Figure 6). 'Plug-scale layering' is also observed in the B33 sample because of alternate porosity and permeability variations. However, this effect is not apparent when looking at the physical sample.

Table 2: Example of uncertainty from segmentation methods.

	B11				B23			
	Kx (md)	Ky (md)	Kz (md)	Porosity (%)	Kx (md)	Ky (md)	Kz (md)	Porosity (%)
DEFAULT	3.19	1.55	30.80	22.84	0.64	3.25	23.04	20.58
OTSU	10.03	3.68	69.71	23.54	2.08	13.68	60.77	22.27
WEKA (Low)	0.34	0.22	4.43	8.04	0.17	0.61	10.54	10.79
WEKA (Mid)	8.19	2.89	51.63	18.11	1.16	7.35	34.80	16.02

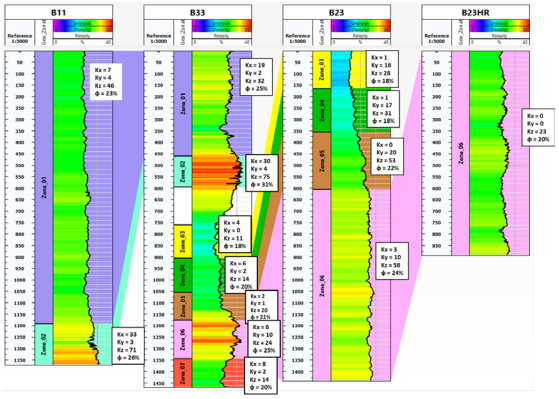

Figure 6: Correlation of calculated porosity across all samples.

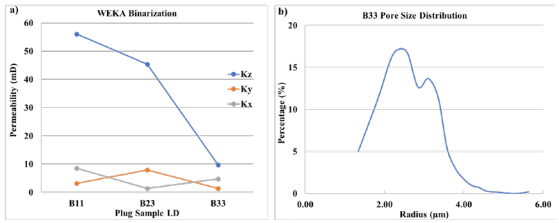

Figure 7: Permeability results from (a) Pore Analysis Tools (PAT) and (b) pore size distribution of B33 sample.

The observed pore-throat structure derived from the image extracted pore network model are characterized by two pore throat frequency peaks with minor differences between them (Figure 7b). The range of properties (porosity, permeability, average pore throat radius) used in categorizing pore throat structures are similar to the wide bimodal type described by (Li, et al., 2020). Good correlation between coordination number and pore radius is observed as smaller pores have smaller coordination numbers.

Porosity and permeability calculations in a Biolithite using x-ray tomography images

Pore Architecture Reconstruction (PAR)

Acquiring x-ray CT data may not always be readily available. Additionally, when the pore geometry becomes more complex, extracting the pore network model might require high performance computers. PAR software stochastically reconstructs realizations of a 3D image using its 2D slices. When realizations of the reconstructed image replicate the pore network geometry and topology (GT), acquisition and processing costs, time and effort will be saved. A short sensitivity analysis on three cases was performed and a summary of the results are in Table 3.

Table 3: Comparison of PAR reconstructed models with original digital images.

	Binarization method		Comment	Sub-volume I.D (and dimensions)	Porosity (PAT)	Kx (md)	Ky (md)	Kz (md)	Extraction Slice no.
INPUT	Otsu	Case 1	Resized Sample	B23_HR (512X512X512)	0.21	0.00	0.00	16.70	N/A
	Otsu	Case 2	GeoZone 1	MASK_B33_New_Otsu_L1 (400X400X400)	0.29	22.91	42.71	4.04	
	Weka	Case 3	Arbitrary subset 2	B33_WEKA_FINAL (670x670x670)	0.14	4.77	2.33	10.21	
OUTPUT	Otsu	Case 1	Resized Model	B23_HR (512X512X512)	0.16	13.25	78.23	174.38	Slice 502
	Otsu	Case 2	GeoZone 1	B33Layer1 (400x400x400)	0.27	49.49	45.12	14.13	Slice 207
	Weka	Case 3	Arbitrary subset 2	OutputB33XY2 (400x400x400)	0.11	1.82	1.17	0.69	Slice 670

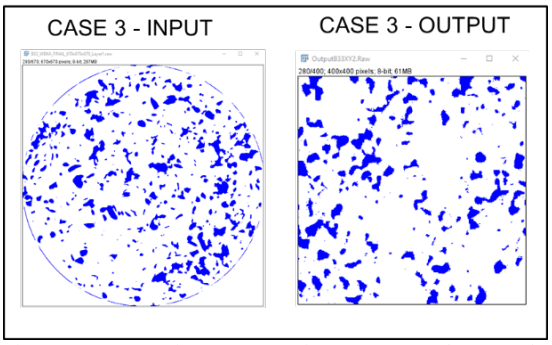

Figure 8: Cross section across B33 input (50µm) and B33 stochastic modeled output – "Case 3". (Blue = pores, and white = matrix)

For case 1 at slice 502, the output model porosity and permeability of B23_HR was not representative. A smoother image was created with more connected pores in the output than the input. Sensitivities on different file setups other than just the default template setup may be necessary to identify suitable parameters for reconstruction of an image.

Case 2 at slice 207, and case 3 at slice 670 (Figure 8) had better comparisons of permeability ranges than case 1. The process of averaging and interpolation when resizing a full stack image introduces uncertainties into the statistics of a resized volume during reconstruction.

Results from Table 3 show that a simplified method that will potentially produce better realizations for this Biolithite sample will be to reconstruct arbitrary volumes from 2D slices within the same zone / layer, preferentially using binarized images generated from machine learning algorithms.

Conclusions

This workflow contributes to an improved sampling strategy in heterogenous pore systems as it enriches the data density and resolution of information that can be derived when characterizing a reservoir using core data. The sub-core scale textural heterogeneities in this Biolithite controls its porosity and permeability distribution. In sample B23, and B11, pore sizes are observed to increase along the height of the sample (the 'depth' axes).

Permeability in three orthogonal directions was calculated for each core plug. K_z is higher than K_x and K_y in all our samples (Table 2). This trend can be explained by the fact that some pores exhibit smaller voids at shallower heights in the sample but become enlarged with increasing depth, as seen in a 3D projection within a smaller region of interest. Anisotropy in the B23 is controlled by preferential orientation of some pores which increased the K_y - component. The lower magnitude of K_z in B33 is believed to be due to the layering effect observed on the derived log.

Upscaling & integration of image analysis derived properties into field-scale 3D reservoir models will help to optimize reservoir management strategies for different applications, *e.g.*, in carbon capture and storage, geothermal energy, monitoring subsurface water contamination, and transport phenomena in geologic disposal of radioactive waste, unconventional and conventional oil & gas applications.

Further work can incorporate results from other techniques such as: mercury injection capillary pressure (MICP), nitrogen gas adsorption, scanning electron microscope (SEM) analysis and corresponding mineralogical interpretation from thin section analysis, etc. to complement the results presented based on this image analysis workflow.

Acknowledgements

Adetomiwa Aderemi gratefully acknowledges the Petroleum Technology Development Fund (PTDF) Nigeria for the funding provided and Heriot-Watt University Institute for Geoenergy Engineering for their invaluable support up till the successful completion of the initial phase of this work.